Composite Structures 287 (2022) 115364

Contents lists available at ScienceDirect

Composite Structures

journal homepage: www.elsevier.com/locate/compstruct

A dynamic finite element procedure for bending collapse of composite thin-walled lenticular tubes

Qilong Jia [a], Ning An [b,*], Xiaofei Ma [c], Jinxiong Zhou [a]

[a] State Key Laboratory for Strength and Vibration of Mechanical Structures and School of Aerospace, Xi'an Jiaotong University, Xi'an 710049, People's Republic of China

[b] School of Aeronautics and Astronautics, Sichuan University, Chengdu 610065, People's Republic of China

[c] Xi'an Institute of Space Radio Technology, Xi'an 710100, People's Republic of China

ARTICLE INFO

Dataset link: https://github.com/Dr-Ning-An/bending-collapse-CTLTs

Keywords:
Wrinkling
Collapse
Pure bending
Finite element method
Composite thin-walled tubes

ABSTRACT

This paper presents an explicit dynamic procedure based finite element framework to investigate the quasi-static bending collapse behavior of composite thin-walled lenticular tubes (CTLTs). A detailed description of the boundary conditions and loads adopted for pure bending tests, and of determining appropriate analysis parameters that control the quasi-static process, such as the simulation time duration and damping coefficient, is given with simulation tests. The quasi-static condition is ensured by using energy balance assessments and the accuracy of the results is verified against true static simulation results reported previously. The collapse performances of a particular CTLT were evaluated numerically in two bending directions. Two distinct regimes were observed, namely, a pre-collapse regime and a post-collapse regime, and the collapse peak moment and critical bending angle that mark the division of the two regimes were predicted. It is shown that as the bending angle increases progressively, the CTLT first bends and buckles into periodic wrinkling patterns at the locally compressed region in the pre-collapse stage, and then after collapsing into the post-collapse stage, the bending moment drops rapidly and the wrinkling patterns evolve into localized ridges and folds, and finally the deformation is concentrated at a certain position of the compressed region.

1. Introduction

The composite thin-walled lenticular tube (CTLT) is a deployable boom structure consists of joined two thin omega-shaped cylindrical shells forming a closed lenticular section as shown in Figs. 1a and 1b. Its cross-sectional geometry allows it to be easily flattened and coiled in a small volume before and during launch, and capable of deploying passively by releasing the stored strain energy for use once in orbit. Given the superior structural performance capabilities amongst other thin-shell deployable boom designs, the thin-walled lenticular tubes or booms have been developed and employed as a basic component to construct various large space structures since its invention in 1960s [1]. Application examples of CTLTs in space include wrapped-rib antenna developed by Oxford Space System Ltd (OSS) in UK [2], solar propelled sailcraft demonstrated by European Space Agency ESA and German Aerospace Center DLR [3] and solar sail supporter for NASA's deep space science and exploration missions on CubeSat platforms [4,5]. Aerospace scientists and engineers in China have also been conducting many fundamental research to study the flattening and wrapping process of CTLTs in recent years [6–8], although none has yet been demonstrated in space.

In a very recent work, we have investigated the nonlinear buckling and post-buckling behavior of CTLTs under pure bending [9]. The nonlinear critical buckling load and post-buckling response of CTLTs were predicted by a numerical scheme that combines eigenvalue buckling analysis and nonlinear static analysis in Abaqus/Standard. A typical moment–angle curve for the pure bending test of the CTLT is shown in Fig. 1c. There are two regimes observed on the curve, namely, a pre-buckling regime and a stable post-buckling regime, and the transition point between the two regimes is identified as the critical buckling point. At the end of the post-buckling regime, the Newton–Raphson implicit method for nonlinear static analysis in Abaqus/Standard appears to be diverging and it was considered that the limit point of collapse is reached [10–12]. Therefore, our research questions are following: (i) is the moment at the end of the post-buckling regime the 'true' peak collapse moment? (ii) how does the CTLT behave if the applied bending angle is increased continuously to beyond the limit point? Clear answers to these questions are apparently important for the evaluation of the effective load-carrying capability of CTLTs. To answer these questions it is required to examine the complete bending

* Corresponding author.
E-mail address: anning@scu.edu.cn (N. An).

https://doi.org/10.1016/j.compstruct.2022.115364
Received 7 April 2021; Received in revised form 29 January 2022; Accepted 4 February 2022
Available online 18 February 2022

collapse behavior of the CTLT and collect moment and angle data at both pre-collapse and post-collapse stages [13,14].

The bending collapse behavior involved with buckling and wrinkling instabilities of thin-walled tubes can be properly captured by the means of both experiments and numerical simulations. Through a non-contact measurement system, Tao and Wang et al. [15,16] experimentally observed the wrinkling evolution and collapse behavior of a mesh reinforced membrane inflated beam and reported an improvement on the load-carrying capability by wrinkling control of the beam. Yuan et al. [17] developed a finite element model for evaluating the extent to which carbon steel lined pipe can be bent before liner collapse, and reported that the liner at the compressed side first wrinkles and at higher curvature buckles and collapses in a diamond shaped mode. Houliara et al. [18] proposed a simple analytical model for analyzing the buckling behavior of long thin-walled steel tubes by considering the ovalized pre-buckling configuration and derived useful closed-form expressions. Yadav et al. [19] numerically investigated the buckling behavior and imperfection sensitivity of thin steel cylindrical shells under pure bending, studied the inelastic localized buckling instability and revealed the impact of steel strain-hardening models on the bending collapse behavior. Limam et al. [20] investigated the inelastic bending and collapse behavior of tubes in the presence of internal pressure through combined experiments and simulations.

The bending collapse has also been considered as an important energy absorption mechanism in automobile and aerospace industry. A large number of studies have been carried out on the bending collapse of thin-walled composite structures with goal to assess crashworthiness and safety of vehicles. For example, Duarte et al. [21] experimentally studied the dynamic and quasi-static three-point bending responses of foam-filled tube structures, and discovered that in comparison to the empty tube and the foam filler, filled tube structure has higher load carrying capacity and much higher energy absorption efficiency. Shin et al. [22] experimentally investigated the energy absorption capability of axial crush and bending collapse of aluminum/GFRP hybrid tubes. Chen et al. [23] evaluated the quasi-static bending crushing performance of hat-shaped composite tubes made of CFRP, GFRP and their hybrid structures through a series of experimental tests. Huang et al. [24] combined experiments and simulations to investigate the bending collapse and crashworthiness of the multi-cell aluminum/CFRP hybrid tubes under quasi-static and dynamic loading. However, most of previous studies on bending collapse behavior of thin-walled tubes have considered cylindrical tubes with regular cross-sections such as circles or squares. The wrinkling and collapse behavior of thin-walled cylindrical structures made of laminates with more complex cross-section like the lenticular shape shown in Fig. 1b remain largely unexplored, and the only closely related study reported by Sickinger et al. [3] focuses only on the post-collapse behavior of a CTLT boom but ignores the evolution of wrinkling patterns in the loading process.

The aim of this study is to evaluate the load-carrying capability of the CTLT throughout the entire bending collapse process with focus on the wrinkling evolution in the post-collapse stage. The bending collapse process is involved with complex unstable post-buckling and collapse problems and in such problems there are expected complicated contact and significant discontinuities that were not possible to be solved by iteration with implicit methods [25]. To properly capture the post-collapse instability, we include inertia effects by adopting a dynamic finite element procedure and solve the bending collapse problem explicitly in a quasi-static manner [26–28]. First, we perform a variety of sensitivity studies to determine the appropriate simulation parameters that ensure a quasi-static loading process with a minimal computational cost. The increase in the duration of simulation time and the amount of numerical damping shows effectiveness on the suppression of dynamic oscillations of the structure, resulting in quasi-static results. With the numerical model in hand, we then analyze the entire bending collapsing response of the CTLT in two directions. It is shown that the CTLT first bends and buckles into periodic wrinkling patterns at the compressed region at small applied bending angles. Then, as the bending angle increases continuously to beyond the limit point, the reaction moment drops rapidly and the wrinkling patterns quickly evolve into localized ridges. Finally, the CTLT folds at a certain position of the compressed region and the moment falls into a low value range.

Table 1
Geometric parameters of the CTLT.

Parameter	Value [mm]
l	504
t	0.071
R	5.354
w	1.0
L	3.0

The paper is organized as follows. Section 2 outlines the finite element model implementation and illustrates the boundary conditions and loads adopted for the pure bending tests. Section 3 concludes the key simulation techniques in Abaqus/Explicit for conducting a quasi-static analysis. Section 4 introduces the methods that are used to determine the appropriate simulation parameters in the model; these parameters include the simulation time, damping coefficient and filter cut-off frequency. Section 5 presents the bending collapse response results obtained from the quasi-static simulation, highlighting the evolution from distributed periodic wrinkling to localized ridges and folds. Finally, concluding remarks are included in Section 6.

2. Finite element model

As depicted in Fig. 1, the geometry of the CTLT is fully characterized by the longitudinal length l, thin-shell thickness t, and the cross-section parameters: web width w, lumbus length L, and circular arc radius R. A set of geometric parameters as in Table 1 are chosen to optimize the bending resistance performance as reported in our recent work [9]. Moreover, in accordance with previously reported experimental data [10], each omega-shaped shell is comprised of four layers of unidirectional carbon fibers that are arranged in the stacking sequence of $[0°, 90°]_S$ in an epoxy resin. The nominal orthotropic elastic material properties of each layer are set as $E_1 = 128.0$ GPa, $E_2 = 6.5$ GPa, $\nu_{12} = 0.35$, $G_{12} = G_{13} = G_{23} = 7.5$ GPa, and the density of the laminates is 1.2 g/cm^3.

Finite element models were constructed using four-node reduced integration general-purpose shell elements with enhanced hourglass control (element type S4R) in the commercial code Abaqus 2020. Fig. 2 presents a finite element mesh representation with boundary conditions for the pure bending problem. Rigid cross-sections are formed by kinematically coupling the nodes at the two end cross-sections to two reference points, A and B, respectively. All degrees of freedom at nodes A and B are restrained, except the translation along z-axis and rotation about the bending axis (about which bending is to take place). The translational degrees of freedom along z-axis of nodes A and B are then correlated to each other by the command *Equation as $U_Z^A + U_Z^B = 0$, and the rotational degrees of freedom about the bending axis of nodes A and B are correlated to a dummy node C as $UR_X^A - UR_X^B = UR_X^C$ for bending about x-axis and $UR_Y^A - UR_Y^B = UR_Y^C$ for bending about y-axis. To induce pure bending to the CTLT steadily, UR^C was increased in a smooth manner from 0 to 0.2 rad over a prescribed step time duration using the Abaqus command *Amplitude, definition=smooth step. The response of the CTLT was simulated by conducting nonlinear explicit dynamic simulations and quasi-static conditions were ensured by introducing a small amount of numerical damping and by monitoring the kinetic energy. Moreover, the composite material behavior was captured with a composite shell section by specifying the material properties, thickness, and orientation angle of each lamina layer in Abaqus. In addition, to handle possible interactions during collapse between different parts of the CTLT, the general contact algorithm in Abaqus/Explicit was adopted and a frictionless contact property was assumed [28].

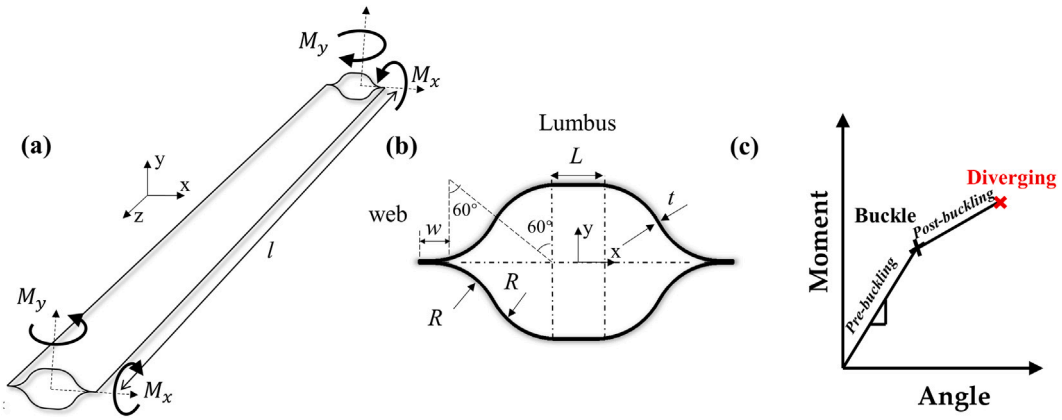

Fig. 1. Schematic of the CTLT with circular arcs. (a) A CTLT in the deployed, i.e., unstressed configuration. (b) Cross-section of the CTLT with geometric parameters indicated. The values for these parameters are given in Table 1. (c) Typical post-buckling response of the CTLT when subjected to a pure bending load obtained with Abaqus/Standard [9].

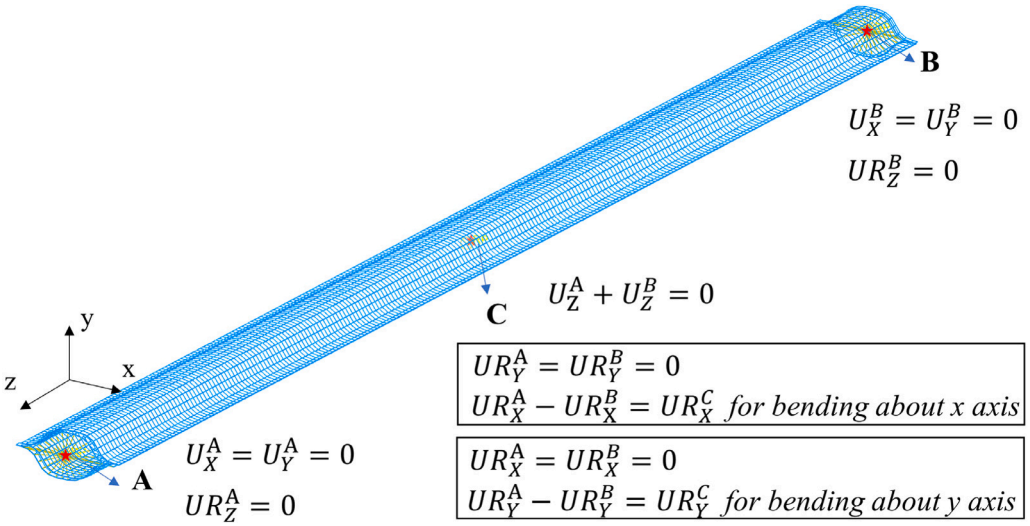

Fig. 2. Finite element model of the CTLT with a coarse mesh representation for visualization purpose.

3. Simulation techniques in Abaqus/Explicit

3.1. Dynamic analysis with Abaqus/Explicit

The explicit solution method is a true dynamic procedure that was originally developed to analyze high-speed dynamic problems where inertia plays a dominate role in the solution. The equilibrium equation of a dynamic analysis discretized in finite elements can be given as follows:

$$\mathbf{M}\ddot{\mathbf{U}} + \mathbf{C}\dot{\mathbf{U}} + \mathbf{K}\mathbf{U} = \mathbf{F}(\mathbf{t}) \tag{1}$$

where **M** is the mass matrix, **C** is the damping matrix, **K** is the stiffness matrix, **F**(**t**) is the vector of external forces, and the vectors of displacement, velocity and acceleration are given by **U**, $\dot{\mathbf{U}}$ and $\ddot{\mathbf{U}}$, respectively.

Abaqus/Explicit uses a central difference rule to integrate the equations of motion explicitly through time, which uses the kinematic conditions at one increment to calculate the kinematic conditions at the next increment. First, the accelerations are assumed to be constant throughout an instant increment and they are integrated through time to calculate the change in velocities. This change in velocities are added to the velocities from the middle of the previous increment to determine the velocities at the middle of the current increment:

$$\dot{\mathbf{U}}\,|_{(t+\frac{\Delta t}{2})} = \dot{\mathbf{U}}\,|_{(t-\frac{\Delta t}{2})} + \frac{\Delta t\,|_{(t+\Delta t)} + \Delta t\,|_{(t)}}{2}\ddot{\mathbf{U}}\,|_{(t)} \tag{2}$$

Then, the velocities are integrated through time and added to the displacements at the beginning of the increment to determine the displacements at the end of the increment:

$$\mathbf{U}\,|_{(t+\Delta t)} = \mathbf{U}\,|_{(t)} + \Delta t\,|_{(t+\Delta t)}\,\dot{\mathbf{U}}\,|_{(t+\frac{\Delta t}{2})} \tag{3}$$

Therefore, the dynamic problem can be solved by the following procedure: (i) satisfying the dynamic equilibrium equation, i.e., Eq. (1) at the beginning of the increment provides the accelerations; and (ii) knowing the accelerations, the velocities and displacements are advanced "explicitly" through time by Eqs. (2) and (3). The term "explicit" refers to the fact that Abaqus/Explicit determines the solution without iterating by explicitly advancing the kinematic state from the displacements, velocities and accelerations at the end of the previous increment. This feature offers certain advantages for solving complex unstable post-buckling and collapse problems, as in such problems there are expected complicated contact and significant discontinuities and it may not be possible to obtain an efficient solution by iteration with implicit methods. On the other hand, with the explicit method the state of the model is advanced through an increment of time, Δt, based on the state of the model at the start of the increment at t. To ensure an accurate and stable representation of the problem, the size of the time increment Δt must satisfy the Courant condition, namely, the time increment cannot be larger than the time for an elastic wave to travel between adjacent nodes in the finite element mesh [26]. Based on the element-by-element estimate, the *stability limit* can be approximated

using the characteristic element length, L^e, and the wave speed of the material, c_d:

$$\Delta t_{stable} = \frac{L^e}{c_d} \tag{4}$$

where c_d is a property of the material which can be estimated by Young's modulus E and material density ρ as follows:

$$c_d \approx \sqrt{\frac{E}{\rho}} \tag{5}$$

3.2. Quasi-static analysis with Abaqus/Explicit

The explicit solution method has also proven valuable in solving quasi-static problems and there are some special considerations that need to be addressed to leverage the trade-off between accuracy and efficiency. Ideally, if the dynamic problem is analyzed over a long enough time scale, the terms related to velocity and acceleration in Eq. (1) vanish and the dynamic equilibrium equation would reduce to a quasi-static equilibrium equation as following:

$$\cancel{\mathbf{M}}\ddot{\mathbf{U}} + \cancel{\mathbf{C}}\dot{\mathbf{U}} + \mathbf{K}\mathbf{U} = \mathbf{F}(\mathbf{t}) \tag{6}$$

However, it is often computationally impracticable to simulate an event in its naturally long time scale, which would require an excessive number of small time increments. Note that for a given model with a specified finite element mesh and material properties, the *stability limit* of explicit time increment is predetermined as described by Eqs. (4) and (5), and thus the increase in simulation time would lead to a proportional increase in the computational cost. Therefore, in practice, the objective of quasi-static analysis is to model the process in the shortest time period in which inertial forces remain insignificant. To achieve this objective efficiently, additional damping is usually introduced into the model to dissipate energy build-up at high frequencies and to avoid sudden failure of elements due to large out-balance forces that may develop at few local distorted region [26]. In this study we consider two kinds of numerical damping: *bulk viscosity* and *viscous pressure*. *Bulk viscosity* introduces a volumetric strain rate-dependent pressure, p_{bv}, and a curvature strain rate-dependent moment, m_{bv}, for all shell elements as following:

$$p_{bv} = b_1 \rho c_d L^e \dot{\epsilon}_{vol} \quad \text{and} \quad m_{bv} = b_1 \frac{h_0^2}{12} \rho c_d L \dot{\kappa} \tag{7}$$

where b_1 is a damping coefficient (default = .06), $\dot{\epsilon}_{vol}$ is the volumetric strain rate, h_0 is the initial thickness, and $\dot{\kappa}$ is twice the mean curvature strain rate. *Viscous pressure* introduces a velocity-dependent normal pressure, p_{vp}, on the shell elements, which can be expressed as:

$$p_{vp} = -c_v(\tilde{\mathbf{v}} \cdot \tilde{\mathbf{n}}) \tag{8}$$

where c_v is the viscous pressure coefficient and usually set to a small percentage of the quantity ρc_d, $\tilde{\mathbf{v}}$ is the velocity vector of the point on the surface where the viscous pressure is being applied, and $\tilde{\mathbf{n}}$ is the unit outward normal vector to the surface at the same point.

The amount of damping should be as small as possible to avoid influencing the simulation results while providing an effective capability to keep the dynamic oscillations at low level. The monitoring of the variation of various model energies, in effect, provides the most general means of evaluating whether or not a simulation is yielding an appropriate quasi-static response [26–28]. The energy balance, which is also referred to as total energy E_{tot} in Abaqus, is defined as the difference between the energy stored in the structure and/or dissipated during the loading process and the work of all external forces. The following is the energy balance equation in Abaqus/Explicit:

$$E_{tot} = E_i + E_v + E_k - E_w \tag{9}$$

where E_i is the internal energy, which is equal to the sum of strain energy and artificial strain energy, E_v is the energy dissipated by viscous damping, E_k is the kinetic energy, and E_w is the work done by the externally applied loads. Quasi-static conditions can be ensured by means of two main checks on the energies in our work. First, the energy balance should remain constant ≈0 since in all the simulations the CTLT was deformed by an external work performed by the prescribed rotations and no other kinds of energy (e.g., thermal) was introduced. Second, the kinetic energy should not exceed a small fraction (typically 5% to 10%) of the internal energy throughout most of the process.

We would like to note that, in this study, a second method for verifying the quasi-static response of the CTLT was provided by comparing the Abaqus/Explicit quasi-static results to the true static simulation results reported previously [9].

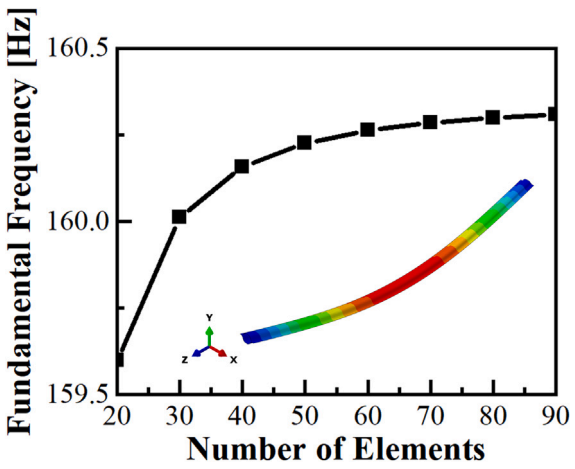

Fig. 3. Convergence analysis of the fundamental frequency results in a mesh refinement study, showing that the fundamental frequency converges to a value of $F \approx 160.2$ Hz at a mesh density of 50 elements along the cross-section profile of the CTLT.

4. Setting the simulation parameters

This section presents a variety of sensitivity studies to determine a set of simulation parameters such as the simulation time and the viscous damping coefficient that provide accurate results and minimal computational cost for quasi-static simulations with Abaqus/Explicit. These studies were mainly focused on the collapse analysis of the CTLT under pure bending about x-axis, but the procedure can be readily extended to simulate the response when it is subjected to pure bending about y-axis.

We start by determining an appropriate simulation time, T. The quasi-static response of the CTLT is mainly dominated by its lowest frequency mode, thus the simulation time required to obtain the proper static response can be estimated from the fundamental natural period of vibration of the CTLT. The fundamental natural frequency of the CTLT was extracted by performing an eigenvalue frequency analysis with Abaqus/Standard. A mesh refinement study was conducted for the convergence of fundamental frequency results, as shown in Fig. 3, resulting in a fundamental frequency of $F \approx 160.2$ Hz and a relative mesh density of around 50 elements along the cross-section profile of the CTLT. Then the fundamental natural period of the CTLT can be readily obtained by $T_0 = 1/F = 0.0063$ s. Abaqus/Explicit recommends that the simulation time should be set to more than ten times the fundamental natural period of a structure to simulate a quasi-static process [6]. In order to determine an appropriate simulation time we performed a series of tests with various simulation time as $10T_0$, $20T_0$, $30T_0$ and $40T_0$, and the results are presented in Fig. 4. As can be seen in Fig. 4a that the moment–angle curves for all tests are smooth and almost overlap with each other in the pre-collapse stage, but shows different fluctuation trends in the post-collapse stage. The fluctuations on the curves correspond to the dynamic oscillations occurred in the

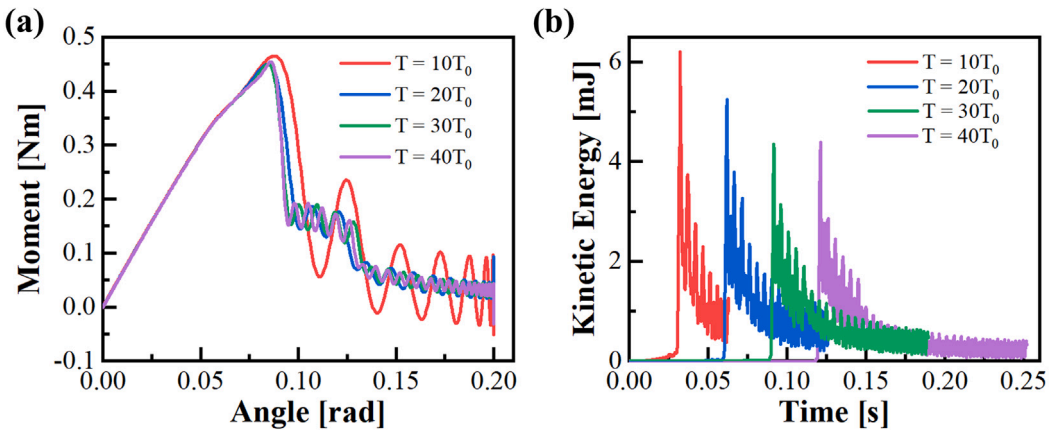

Fig. 4. Sensitivity of (a) moment–angle response and (b) kinematic energy history to explicit simulation step time T.

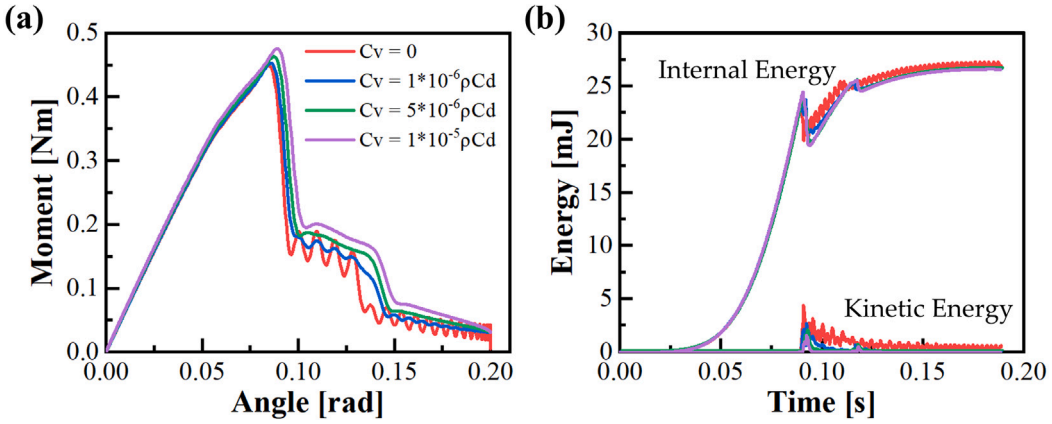

Fig. 5. Sensitivity of (a) moment–angle response and (b) energy history (i.e., internal energy and kinetic energy) to viscous damping coefficient used in the model with a simulation time of $30T_0$.

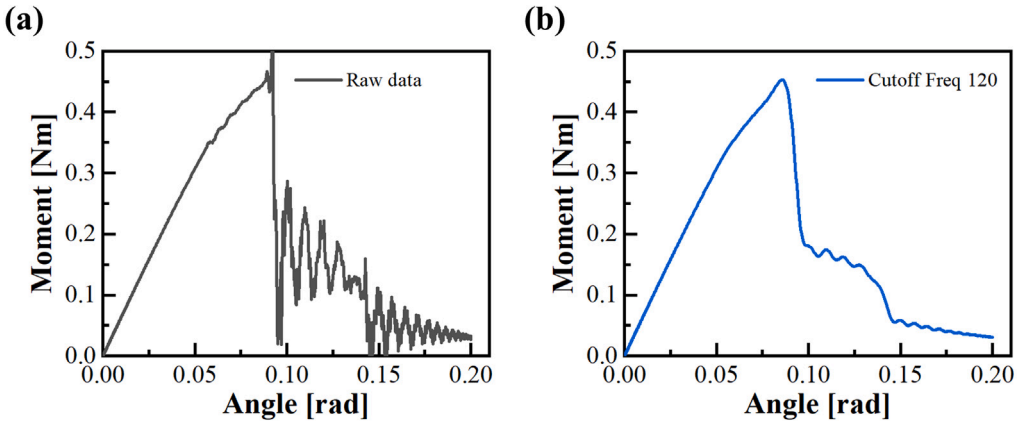

Fig. 6. Simulation results of a FE model characterized by $T = 30T_0$ and $c_v = 1 \times 10^{-6} \rho c_d$. (a) Raw data and (b) filtered data using a Butterworth filter with a cutoff frequency of 120 Hz.

post-collapse stage, and the duration of simulation time plays an important role in controlling these fluctuations. Specifically, the longer is the simulation time, the higher is the fluctuating frequency, and the lower is the fluctuating amplitude. As the simulation time increases, the reduce in the fluctuating amplitude is also manifested by the reduce in the structural kinetic energy during the process, as indicated in Fig. 4b. However, it is also obvious that the fluctuations could hardly be fully eliminated by just increasing the duration of the simulation time. Thus, the duration of $T = 30T_0$ is selected as an appropriate simulation time and further reduce in dynamic oscillations requires the use of additional numerical damping.

We then move on to investigate the sensitivity of the response to the amount of numerical damping introduced to the model. As mentioned in Section 3.2, two kinds of numerical damping were used in our simulations which are *bulk viscosity* and *viscous pressure*. *Bulk viscosity* introduces damping associated with volumetric straining of which the common purpose is to improve the modeling of high-speed dynamic events rather than quasi-static events [29], and thus the default damping coefficient for *bulk viscosity* in Abaqus/Explicit was adopted. On

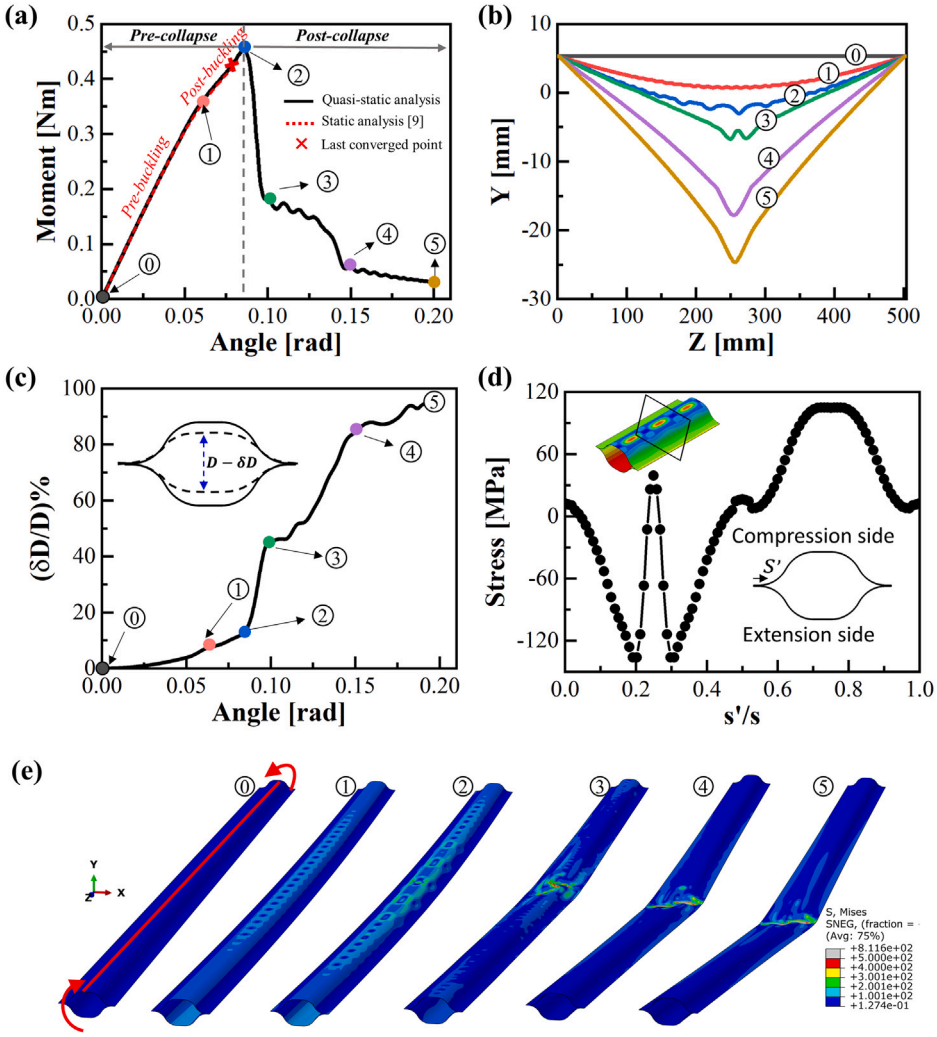

Fig. 7. Wrinkling and collapse response of the CTLT when subjected to a pure bending load about x-axis. (a) Moment–angle curves predicted by Abaqus/Explicit quasi-static analysis with $T = 30T_0$ and $c_v = 1 \times 10^{-6}\rho c_d$ (black solid line) and by Abaqus/Standard true static analysis (red dashed line) [9]. (b) Deformation profiles of the middle line of the compressed lumbus as indicated by the red line shown in ⓪ of (e). (c) Evolution of the flattening deformation of the cross-section at the folding region as a function of the applied bending angle. (d) Axial stress distribution on cross-section at collapsing state ② as denoted in (a). (e) FE deformation snapshots of stress distribution for the CTLT at various stages of loading process.

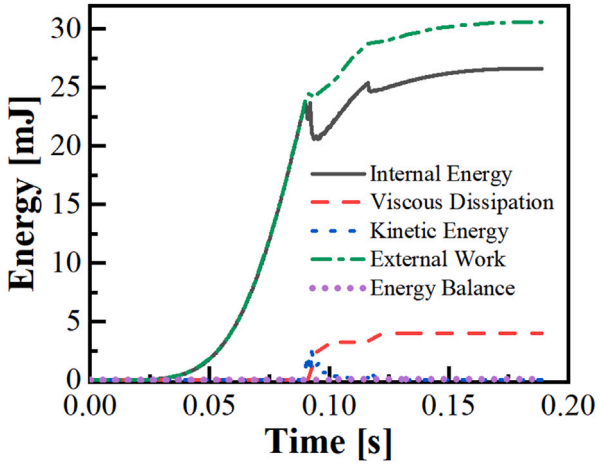

Fig. 8. Energy histories for the quasi-static bending collapse analysis about x-axis with simulation parameters $T = 30T_0'$ and $c_v = 1 \times 10^{-6}\rho c_d$.

the other hand, the damping coefficient for *viscous pressure*, c_v, was determined through a series of simulation tests. Fig. 5 gives the analyses results of FE model with a specified simulation time of $30T_0$ and various viscous pressure damping coefficients, i.e., $c_v = 0$, $1 \times 10^{-6}\rho c_d$, $5 \times 10^{-6}\rho c_d$, $1 \times 10^{-5}\rho c_d$. It can been seen from Fig. 5a that the fluctuations in the post-collapse stage are properly eliminated by the introduction of an viscous pressure with the damping coefficient exceeding $1 \times 10^{-6}\rho c_d$. Fig. 5b shows that the introduction of additional numerical damping undoubtedly reduce the amount of the kinetic energy and thus help keep the ratio of kinetic energy to internal energy low during the loading process.

Finally, we would like to point out that all the moment and angle data reported in this study are filtered by a second-order low pass Butterworth filter coded by a Python script. There is significant noise in the raw data because Abaqus/Explicit simulates a quasi-static response instead of a true static response, see Fig. 6a. Applying Butterworth filtering with an appropriate cutoff frequency [30] could help remove simulation noise and obtain the underlying physical solution, see Fig. 6b.

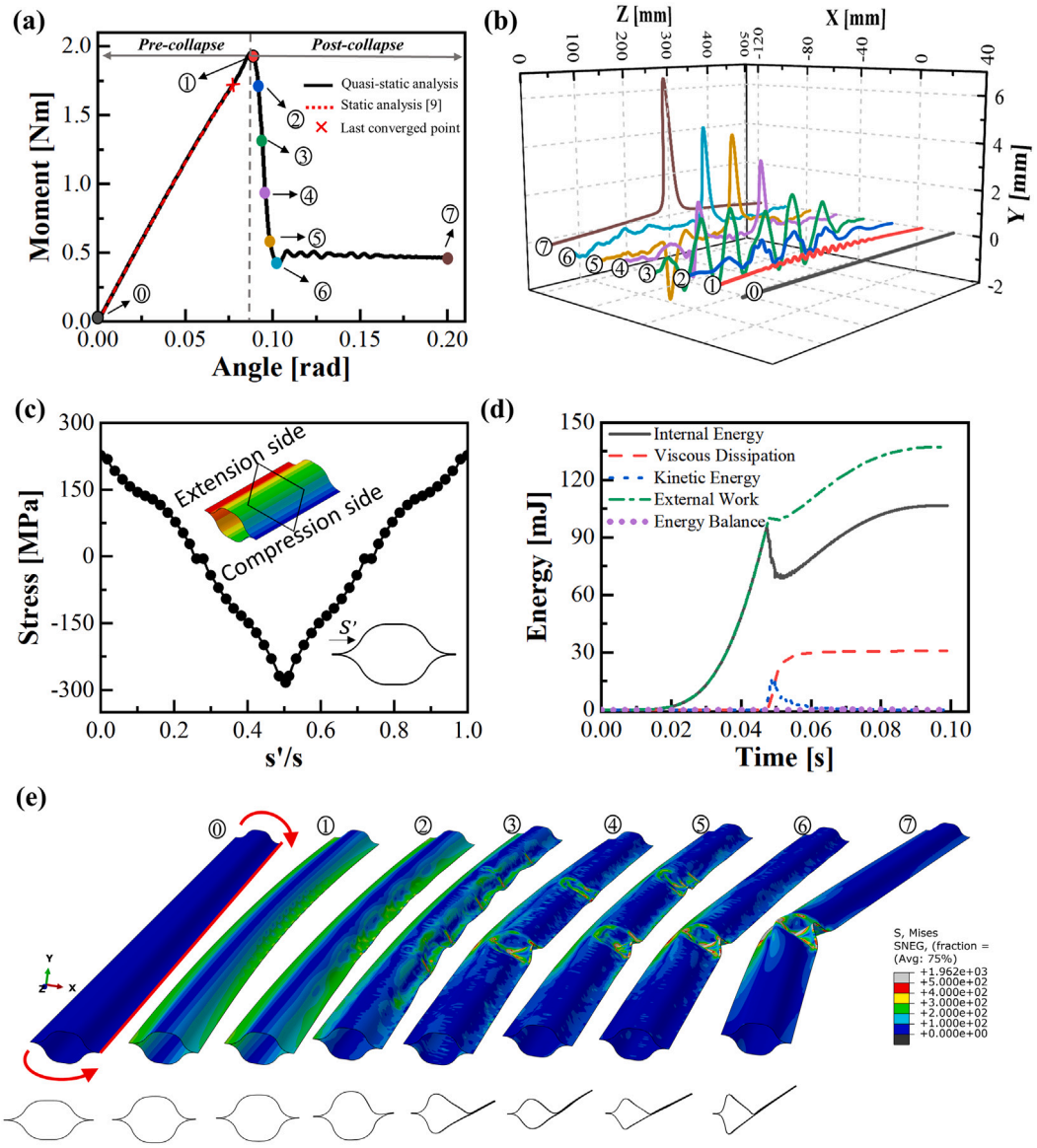

Fig. 9. Wrinkling and collapse response of the CTLT when subjected to a pure bending load about y-axis. (a) Moment–angle curves predicted by Abaqus/Explicit quasi-static analysis with $T = 30T_0'$ and $c_v = 1 \times 10^{-6}\rho c_d$ (black solid line) and by Abaqus/Standard true static analysis (red dashed line) [9]. (b) Deformation profiles at the compressed web edge as indicated by the red line shown in ⓪ of (e). (c) Axial stress distribution on cross-section at collapsing state ① as denoted in (a). (d) Energy histories for the whole bending collapse process. (e) FE deformation snapshots of stress distribution for the CTLT at various stages of loading process. The images in bottom panel indicate the evolution of the cross-section at the folding region during the loading process.

5. Results and discussion

Fig. 7 gives the simulation results for the CTLT under a pure bending load about x-axis. It can be firstly observed that there exist two sharply distinct regimes in the complete moment–angle curve (see black solid line in Fig. 7a), namely, a pre-collapse regime and a post-collapse regime. The pre-collapse regime is characterized by a positive stiffness whereas the post-collapse regime is characterized by a negative stiffness. In addition, the pre-collapse regime is further comprised of a pre-buckling region and a stable post-buckling region which are divided by the critical buckling point, and in pre-collapse regime the results predicted by Abaqus/Explicit quasi-static analysis are in an excellent agreement with those obtained by preforming a conventional true static post-buckling analysis in Abaqus/Standard as reported previously [9]. It should also be noted that, the last converged point identified from the true static post-buckling analysis, as indicated by the red cross in Fig. 7a, is not the exact division between the pre- and post-collapse stages, and therefore it is not the 'true' collapse point. One possible explanation for this discrepancy is that when performing the static post-buckling analysis it is inevitable to introduce imperfection in the geometry to guide the deformation. Thus the last converged point is expected to be imperfection-sensitive. On the other hand, one of the advantages of using explicit dynamic procedure is no geometric imperfection is required in the analysis. Therefore we conclude that the 'true' collapse point could only be predicted from the division between the pre- and post-collapse stages by performing a complete bending collapse analysis. To understand collapse phenomena in detail, six points from ⓪ to ⑤ are identified in the moment–angle diagram as shown in Fig. 7a. These points represent six distinct states of the loading process, and the deformation patterns of middle line at the compressed lumbus of the CTLT (as indicated by red solid line shown in ⓪ of Fig. 7e) for these states are included in Fig. 7b. At state ⓪, no rotation is applied and thus the line is in the initial straight shape. At state ①, the line bends upwards and periodic winkling patterns can be observed. This is a clear sign of the buckling. At state ②, the bending moment reaches its peak value of ≈0.45 Nm, and both the wrinkling wavelength

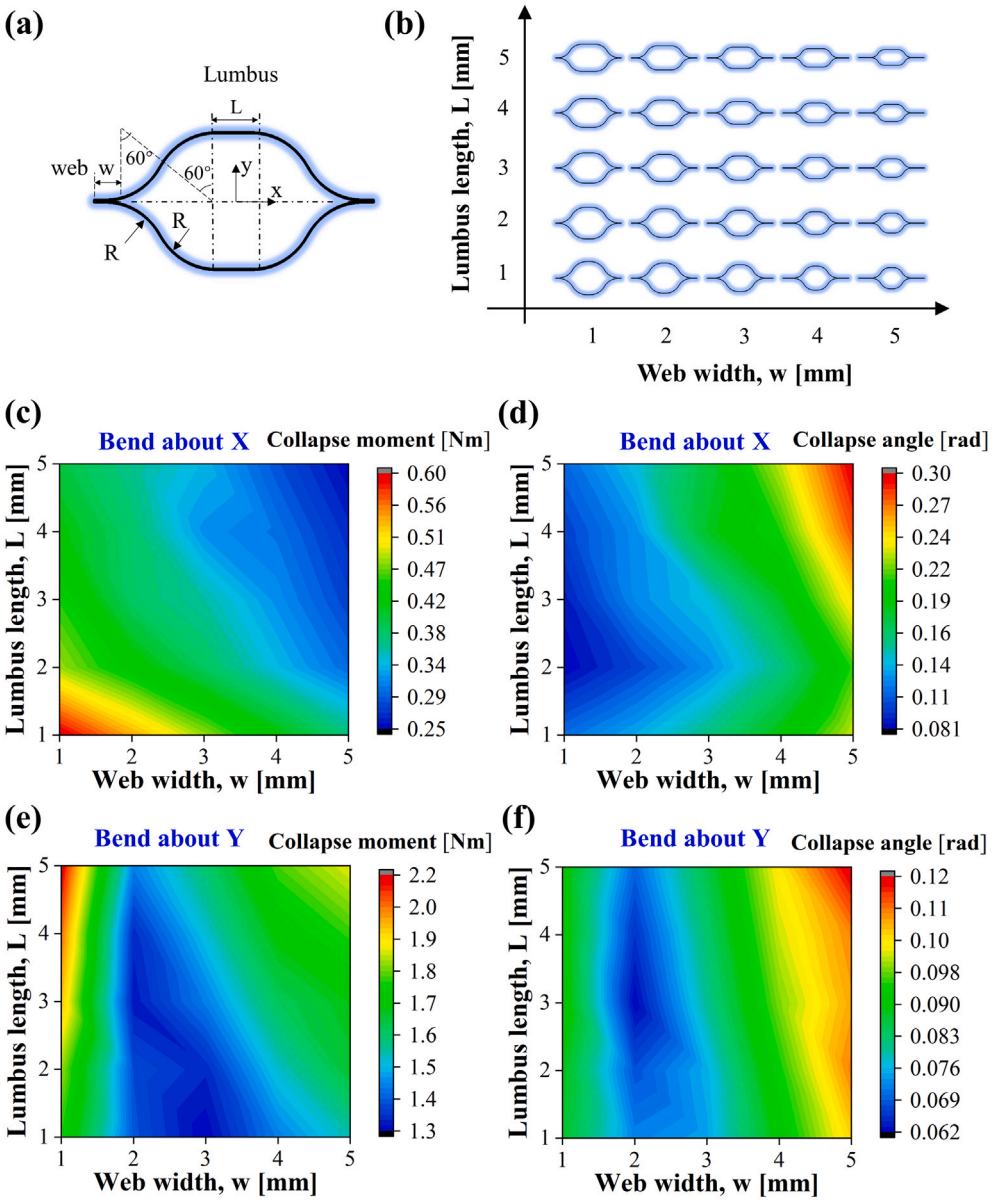

Fig. 10. The design space for bending collapse of CTLTs. (a) Schematic illustration of the cross-section geometry of the CTLT. (b) A variety of cross-section shapes of CTLTs characterized by web width $w \in [1,5]$ mm and lumbus length $L \in [1,5]$ mm. Heat maps illustrating the (c) collapse peak moment and (d) collapse critical bending angle as a function of the web width w and lumbus length L when the moment is applied about x-axis. Heat maps illustrating the (e) collapse peak moment and (f) collapse critical bending angle as a function of the web width w and lumbus length L when the moment is applied about y-axis.

and amplitude increase more significantly at center of the line. After collapsing, at state ③, as the bending angle increases continuously, the bending moment decreases dramatically, and the periodic wrinkling patterns disappears, and a local large wrinkle occurs, which indicates the growth of collapsing. Finally, the deformation is concentrated only at the center of the line at state ④ and ⑤. It is also of interest to analyze the Brazier effect [31] closely along with the flattening deformation of the cross-section at the folding region of the CTLT, as can be seen in Fig. 7c. The flattening deformation increases slowly in the pre-collapse regime (from ⓪ to ②), while after the point of collapsing, the cross-section deforms very rapidly into a flattened configuration. Fig. 7d gives the axial stress distribution on the cross-section at collapsing state ② as denoted in Fig. 7a. It is the stress generated at the compression side that leads to buckling and collapse of the thin-walled structures. Fig. 7e presents the FE deformation snapshots of stress distribution for the CTLT at various stages of the loading process, showing that at the first stage of small bending angle, the CTLT bends slightly upwards and as the bending angle increases beyond the collapse point, the CTLT buckles localized at the center eventually. Finally, the energy histories in the loading process are plotted in Fig. 8. The energy balance remains approximately constant ≈0, and the kinetic energy is negligible compared to the internal energy throughout the simulation; hence, the results are essentially quasi-static. The peaks at about 0.093s correspond to the collapse of the CTLT.

The CTLT buckles and collapses in a similar way when subjected to a pure bending load about y-axis. The most striking feature as shown in Fig. 9a is that there exists no stable post-buckling region in the pre-collapse regime, and collapse occurs more quickly in a quite short time period after buckling. Eight points indicated by number bullets from ⓪ to ⑦ that represent various states of the CTLT in the loading process are

identified in the moment–angle diagram in Fig. 9a and the deformation patterns of the compressed web edge for these states are plotted in Fig. 9b. At state ⓪, the web edge is in the initial straight shape. At state ①, the bending moment peaks to a value of ≈1.9 Nm and the web edge bends slightly with periodic wrinkling patterns observed, which is a sign of both buckling and collapsing. After collapsing, the bending moment drops sharply and the wrinkling patterns evolve rapidly into localized ridges with relatively large amplitudes from ① to ⑥. In the end, the deformation is concentrated at a certain position of the web edge at state ⑦. Fig. 9c gives the axial stress distribution on the cross-section at collapsing state ① as denoted in Fig. 9a. Fig. 9d presents the energy histories in the quasi-static bending process of the CTLT about y-axis. The energy balance remained approximately constant ≈ 0 throughout the simulation, which indicates the accuracy of the results. The kinetic energy reaches a peak at about 0.048s which corresponds to the collapse of the CTLT. Fig. 9e gives the FE deformation snapshots of stress distribution for the CTLT at various stages of the loading process. The images in bottom panel indicate the evolution of the cross-section at the folding region during the loading process.

We would like to highlight two points that arising from the quasi-static simulations of the CTLT bent about y-axis. (i) The simulation time in this model is $T = 30T_0'$, where $T_0' = 1/F'$ is the fundamental natural period of the CTLT associated with bending about y-axis, and $F' = 306.9$ Hz was obtained by performing a separate eigenvalue frequency analysis. (ii) The resulted moment–angle responses are identical when Abaqus/Explicit simulation is run in parallel with different number of processors; the wrinkling evolution behavior could be slightly different, though. This generally comes from rounding errors due to the large number of increments required and limited precision of the floating point representation. The double precision executable in Abaqus/Explicit is recommended to profoundly reduce the rounding errors.

Finally, we construct a design space and use simulation to explore the evolution of collapse peak moment and critical bending collapse angle as a function of the cross-section geometry of CTLTs. As schematized in Fig. 10a, the cross-section of CTLT is characterized by three geometric parameters, the web width w, lumbus length L and circular arc radius R. In this work, we introduced a constraint by fixing the perimeter of the lenticular shape as a constant, and therefore a design space was constructed by varying the two independent geometric parameters, the web width w, and lumbus length L, as shown in Fig. 10b. Figs. 10c–f give the evolution of the collapse peak moment and critical bending collapse angle over the design space, for both bending about $x-$ and y-axis. The results shown in Figs. 10c and 10d demonstrate that the bending collapse moment and critical angle about x-axis of CTLTs depend highly on both the web width w and the lumbus length L, while the results reported in Figs. 10e and 10f show that the bending collapse moment and critical angle about y-axis of CTLTs depend strongly on the web width w, but slightly on the lumbus length L. Interestingly, the results also show that the cross-section geometry produced opposite response in terms of bending collapse moment and critical collapse angle. For example, as the web width w increases, the bending collapse moment decreases but the critical collapse angle increases for both bending about $x-$ and y-axis.

6. Concluding remarks

This paper describes an explicit dynamic procedure based on the commercial finite element code, Abaqus, to capture the whole quasi-static collapse response of the CTLT under pure bending. The procedure includes three steps: (i) estimating the fundamental natural period T_0 of the CTLT by performing an eigenvalue frequency analysis; (ii) analyzing the bending collapse response of the CTLT with increasing simulation time starting from $10T_0$ until the fluctuation amplitudes remain nearly unchanged and small; and (iii) introducing a small amount of numerical damping to eliminate the fluctuations by limiting the kinetic energy negligible compared to the internal energy. Additionally, in the whole loading process, the energy balance should be checked to remain constant ≈0, and the raw data produced by the explicit method could be filtered to remove simulation noise and hence obtain the underlying physical solution.

The proposed framework has been applied to evaluate the quasi-static bending collapse performance of the CTLT in two directions. The peak moments during the loading process were obtained which are ≈0.45 Nm in the $x-$direction and ≈1.9 Nm in the $y-$direction. Two distinct regimes are identified from the explicit simulation results, namely, the pre-collapse regime and the post-collapse regime. The behavior of the CTLT can be described as follows: (i) in the pre-collapse regime, the CTLT first bends and then buckles into periodic wrinkling patterns at the compressed region; (ii) after collapsing into the post-collapse regime, the bending moment drops dramatically, and the periodic wrinkling patterns evolve into localized ridges and folds; and (iii) at the end of the bending, the deformation of the CTLT is concentrated at a certain position of the compressed region. Through the construction and exploration of the design space, the effect of cross-section geometry on the bending collapse performance of CTLTs has been revealed, and an inherent trade-off was discovered between the maximum load-carrying capability and the maximum bending angle of CTLTs under pure bending.

We believe our numerical framework provide guidelines for engineers and scientists attempting to examine the quasi-static response of composite thin-walled tubes or booms. Our simulation results throw some light on the bending collapse performance of composite thin-walled lenticular tubes and more experimental observations of these collapse behavior can be expected in future research.

CRediT authorship contribution statement

Qilong Jia: Conceptualization, Methodology. **Ning An:** Software, Investigation, Data curation, Writing – original draft. **Xiaofei Ma:** Resources, Supervision. **Jinxiong Zhou:** Writing – review & editing.

Declaration of competing interest

The authors declare that they have no known competing financial interests or personal relationships that could have appeared to influence the work reported in this paper.

Data availability

The raw/processed data required to reproduce these findings are available to download from [https://github.com/Dr-Ning-An/bending-collapse-CTLTs].

Acknowledgments

This research is supported by the Fundamental Research Funds for the Central Universities, China (No. YJ2021137) and the National Natural Science Foundation of China (No. 11972277). Q. J. also acknowledges the support from Shanghai Rising-Star Program, China (19QB1404000).

References

[1] Rennie BB. New closed tubular extendible boom. In: 2nd aerospace mechanisms symposium. 1967, p. 163–70.
[2] Yoshiro O, Reveles J, Fraux V, Ashley D-J. Deployable wrapped rib assembly. Google Patents; 2019, US Patent App. 16/348, 390.
[3] Sickinger C, Herbeck L, Breitbach E. Structural engineering on deployable CFRP booms for a solar propelled sailcraft. Acta Astronaut 2006;58(4):185–96.
[4] Fernandez JM, Rose GK, Younger CJ, Dean GD, Warren JE, Stohlman OR, et al. NASA'S advanced solar sail propulsion system for low-cost deep space exploration and science missions that use high performance rollable composite booms. 2017.

[5] Fernandez JM, Rose G, Stohlman OR, Younger CJ, Dean GD, Warren JE, et al. An advanced composites-based solar sail system for interplanetary small satellite missions. In: 2018 AIAA spacecraft structures conference. 2018, p. 1437.
[6] Bai J-B, Chen D, Xiong J-J, Shenoi RA. Folding analysis for thin-walled deployable composite boom. Acta Astronaut 2019;159:622–36.
[7] Hu Y, Chen W, Gao J, Hu J, Fang G, Peng F. A study of flattening process of deployable composite thin-walled lenticular tubes under compression and tension. Compos Struct 2017;168:164–77.
[8] Chen W, Fang G, Hu Y. An experimental and numerical study of flattening and wrapping process of deployable composite thin-walled lenticular tubes. Thin-Walled Struct 2017;111:38–47.
[9] Jia Q, An N, Ma X, Zhou J. Exploring the design space for nonlinear buckling of composite thin-walled lenticular tubes under pure bending. Int J Mech Sci 2021;207:106661.
[10] Leclerc C, Wilson LL, Bessa MA, Pellegrino S. Characterization of ultra-thin composite triangular rollable and collapsible booms. In: 4th AIAA spacecraft structures conference. 2017, p. 0172.
[11] Leclerc C, Pellegrino S. Nonlinear elastic buckling of ultra-thin coilable booms. Int J Solids Struct 2020;203:46–56.
[12] STOCKWELL A, COOPER P. Collapse of composite tubes under end moments. In: 33rd structures, structural dynamics and materials conference, p. 2389.
[13] Kecman D. Bending collapse of rectangular and square section tubes. Int J Mech Sci 1983;25(9–10):623–36.
[14] Halgrin J, Haugou G, Markiewicz E, Rota L. Integrated simplified crash modelling approach dedicated to pre-design stage: evaluation on a front car part. Int J Veh Saf 2008;3(1):91–115.
[15] Tao Q, Wang C, Xue Z, Xie Z, Tan H. Wrinkling and collapse of mesh reinforced membrane inflated beam under bending. Acta Astronaut 2016;128:551–9.
[16] Liu Y, Wang C, Tan H, Wadee M. The interactive bending wrinkling behaviour of inflated beams. Proc R Soc A: Math Phys Eng Sci 2016;472(2193):20160504.
[17] Yuan L, Kyriakides S. Liner wrinkling and collapse of bi-material pipe under bending. Int J Solids Struct 2014;51(3–4):599–611.
[18] Houliara S, Karamanos SA. Buckling of thin-walled long steel cylinders subjected to bending. J Press Vessel Technol 2011;133(1).
[19] Yadav KK, Gerasimidis S. Instability of thin steel cylindrical shells under bending. Thin-Walled Struct 2019;137:151–66.
[20] Limam A, Lee L-H, Corona E, Kyriakides S. Inelastic wrinkling and collapse of tubes under combined bending and internal pressure. Int J Mech Sci 2010;52(5):637–47.
[21] Duarte I, Vesenjak M, Krstulović-Opara L. Dynamic and quasi-static bending behaviour of thin-walled aluminium tubes filled with aluminium foam. Compos Struct 2014;109:48–56.
[22] Shin KC, Lee JJ, Kim KH, Song MC, Huh JS. Axial crush and bending collapse of an aluminum/GFRP hybrid square tube and its energy absorption capability. Compos Struct 2002;57(1–4):279–87.
[23] Chen D, Sun G, Jin X, Li Q. Quasi-static bending and transverse crushing behaviors for hat-shaped composite tubes made of CFRP, GFRP and their hybrid structures. Compos Struct 2020;239:111842.
[24] Huang Z, Zhang X, Yang C. Experimental and numerical studies on the bending collapse of multi-cell Aluminum/CFRP hybrid tubes. Composites B 2020;181:107527.
[25] Park HS, Suo Z, Zhou J, Klein PA. A dynamic finite element method for inhomogeneous deformation and electromechanical instability of dielectric elastomer transducers. Int J Solids Struct 2012;49(15–16):2187–94.
[26] Stabile A, Laurenzi S. Coiling dynamic analysis of thin-walled composite deployable boom. Compos Struct 2014;113:429–36.
[27] Mallikarachchi H, Pellegrino S. Optimized designs of composite booms with tape spring hinges. In: 51st AIAA/ASME/ASCE/AHS/ASC structures, structural dynamics, and materials conference 18th AIAA/ASME/AHS adaptive structures conference 12th. 2010, p. 2750.
[28] Mallikarachchi H, Pellegrino S. Design of ultrathin composite self-deployable booms. J Spacecr Rockets 2014;51(6):1811–21.
[29] Sakovsky M, Pellegrino S. Closed cross-section dual-matrix composite hinge for deployable structures. Compos Struct 2019;208:784–95.
[30] Liu X, Belkassem B, Jonet A, Lecompte D, Van Hemelrijck D, Pintelon R, et al. Experimental investigation of energy absorption behaviour of circular carbon/epoxy composite tubes under quasi-static and dynamic crush loading. Compos Struct 2019;227:111266.
[31] Brazier L. On the flexure of thin cylindrical shells and other" thin" sections. Proc R Soc Lond. Series A, Contain Pap Math Phys Character 1927;116(773):104–14.